THE JOURNAL OF PHYSICAL CHEMISTRY C

Article

pubs.acs.org/JPCC

Tunable Photoelectrochemical Properties by Nanostructural Control in WO_3 Thin Films Prepared by Carboxylic Acid-Assisted Electrodeposition

Wai Ling Kwong, Auppatham Nakaruk, Pramod Koshy, and Charles C. Sorrell*

School of Materials Science and Engineering, University of New South Wales, Sydney, NSW 2052 Australia

ABSTRACT: The present work reports the synthesis of transparent (~60−80% transmission) WO_3 thin films by electrodeposition using peroxotungstic acid (PTA) solutions containing different carboxylic acids (formic, oxalic, and citric) of varying concentrations. The effects of these acids on the deposition kinetics and the morphological, mineralogical, optical, and photoelectrochemical properties of the films were investigated using scanning electron microscopy, X-ray diffraction, UV−vis spectrophotometry, and photoelectrochemical measurements. The deposited film thickness was dependent on the availability of hydronium ions (for hydrogen bonding with PTA ions) and molecular drag in the electrolytes, both of which were controlled through the use of carboxylic acids of different concentrations, degrees of dissociation, molecular weights, and associated sizes of the conjugate bases. The films consisted of agglomerates/particles (42−132 nm), the sizes of which decreased and the true porosities (<6%) of which increased with the amounts and sizes of the conjugate bases. These observations were considered to result from the separation of the PTA ions according to the amounts and sizes of the conjugate bases, the effects of which consequently changed the mechanisms of nucleation and grain growth. A nonlinear relationship between the grain sizes and the photoelectrochemical performances of the films was obtained where a maximum in the photocurrent density was observed for the film consisting of small agglomerates of ~93 nm (deposited with 0.03 mol L^{-1} oxalic acid). This was considered to result from the positive balance of (i) surface reaction and recombination sites and (ii) the hole and electron transports in the film.

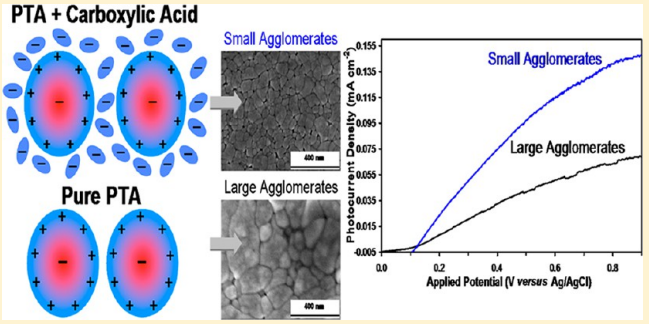

1. INTRODUCTION

Metal oxides have been proven to be suitable for photoelectrochemical applications owing to their high stability in aqueous solutions.[1] WO_3 is an *n*-type semiconductor that has found widespread applications in photocatalysis,[2] gas sensing,[3,4] electrochromism,[5] and electrodes for lithium ion batteries.[6] It is widely considered to be a popular candidate for photoelectrodes for photoelectrochemical cells owing to its high stability against both corrosion and photocorrosion and its relatively smaller optical indirect band gap (compared to TiO_2),[7] which permits limited light absorption in the visible range.[1]

In recent years, there has been an increasing number of studies on photoelectrodes of metal oxide nanomaterials because their advantageous properties,[8] compared to those of their bulk counterparts,[9,10] include large specific surface areas, ease of material synthesis, enhanced photoelectrochemical properties due to suppressed photogenerated electron−hole recombination, and enhanced light absorption.[11] However, reducing the sizes of nanomaterials also may come with adverse effects on their crystallinity and electrical transport properties as a result of the increased grain boundary area and the associated increase in the number of surface defects.[12,13] Thus, it is important to optimize the grain size of WO_3 nanocrystalline thin-film photoelectrodes by controlling the synthesis parameters in order to achieve a compromise between the microstructural parameters and the resultant optical and photoelectrochemical properties, thereby yielding optimal photoelectrochemical performance.

The size-controlled synthesis of WO_3 nanostructures has been reported using various techniques such as hydrothermal,[13] sol−gel,[12,14,15] hot-wire chemical vapor deposition,[16] arc discharge deposition,[4] and radio frequency magnetron sputtering.[17,18] Although some of these techniques require expensive instruments and/or vacuum systems, the sizes of the nanostructures have been controlled principally by thermal treatments at high temperatures (400−950 °C). An alternative to these techniques is organic-compound-assisted wet chemical synthesis. This technique combines the benefits of ecofriendly organic compounds with uncomplicated, economical, and large-area deposition methods. Sun et al. used colloidal processing at high oxalic acid concentrations with tungstenic acid to produce smaller grain sizes and lower crystallinities in WO_3 thin films.[19] Meda et al. reported the size tuning of WO_3 grains prepared by

Received: December 16, 2012
Revised: July 26, 2013
Published: July 26, 2013

 © 2013 American Chemical Society dx.doi.org/10.1021/jp400499c | *J. Phys. Chem. C* 2013, 117, 17766−17776

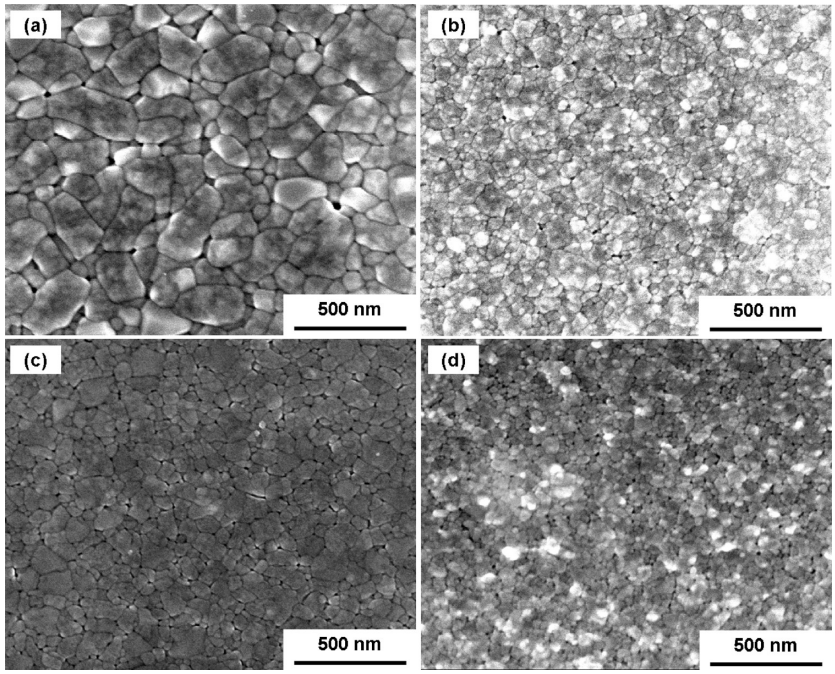

Figure 1. SEM images of WO_3 thin films deposited from (a) pure PTA, (b) PTA with 0.03 mol L^{-1} formic acid, (c) PTA with 0.03 mol L^{-1} oxalic acid, and (d) PTA with 0.03 mol L^{-1} citric acid.

a proton exchange resin method through the addition of various organic dispersants, including ethylene glycol, poly(ethylene glycol), Igepal, Brij, and sugars, where the grain sizes decreased with increasing dispersant molecular weight.[20] Naseri et al. used poly(ethylene glycol) to control the topologies of WO_3 nanocrystalline thin films prepared by a sol−gel method.[21]

There is a limited number of investigations on the size-controlled wet chemical synthesis of WO_3 thin films using organic compounds, and the understanding of the mechanisms associated with the growth of the nanoparticles remains tentative. The present work reports the electrodeposition of WO_3 thin films using peroxotungstic acid (PTA) containing different carboxylic acids of various concentrations in order to investigate the effectiveness of tailoring the grain sizes. The effects of these acids on the electrodeposition kinetics of WO_3 thin films and the resultant morphological, mineralogical, and optical properties were investigated. The correlation and optimization of these properties for photoelectrochemical applications of the films are discussed.

2. EXPERIMENTAL SECTION

2.1. Chemicals. The chemicals used to prepare PTA solutions were tungsten foils (99.99%, Shanghai Leading Metal, China), 30% w/w hydrogen peroxide (analytical reagent, Univar), and propan-2-ol (99.5% analytical reagent, Univar). The carboxylic acids used were formic acid (99% analytical reagent, Asia Pacific Specialty Chemicals), oxalic acid dihydrate (oxalic acid, 99.5% Merck), and citric acid monohydrate (citric acid, 99−102% ACS reagent, Sigma-Aldrich).

2.2. WO_3 Thin Film Preparation. Detailed preparation procedures for PTA solutions have been reported elsewhere.[22] In brief, solutions of PTA with 0.2 mol L^{-1} tungsten containing 0.03 mol L^{-1} carboxylic acid (i.e., formic, oxalic, and citric acids individually) were used as the electrolytes for film deposition. Because optimal results were obtained with the addition of oxalic acid, its effect was studied in detail using concentrations in the range of 0.01 to 0.10 mol L^{-1}. All films were deposited at room temperature using a three-electrode electrochemical system with fluorine-doped tin oxide on glass (FTO; Wuhan Ge'ao Scientific Education Instrument, China; 15 Ω sq^{-1}; 3.0 cm × 2.5 cm), platinum foil, and Ag/AgCl as the working, counter, and reference electrodes, respectively. All potentials reported refer to the reference electrode. The depositions were done at an applied potential of −0.4 V for 5−30 min.[22] The as-deposited films were flushed immediately with distilled water, dried in air for ∼30 min, placed on an aluminosilicate brick, and annealed at 450 °C in air for 2 h (heating and initial cooling rate of 5 °C min^{-1}).

2.3. Characterization. The microstructures of the films were examined using scanning electron microscopy (SEM, FEI Nova NanoSEM) and atomic force microscopy (AFM, Bruker Dimension Icon). The film thicknesses were determined by sectioning the films using single-beam focused ion beam milling (FEI XP200). The true porosities of the films were determined using image analysis (*ImageJ* software, National Institutes of Health). The phase compositions of the films were determined by in situ X-ray powder diffraction (XRD, Philips X'pert Materials Powder Diffractometer) of the films. Light transmission of the films was measured using a dual-beam UV−vis spectrophotometer (Perkin-Elmer Lambda 35).

The photoelectrochemical properties of the films were measured at room temperature using the same electrochemical system as described above but using WO_3 thin films on FTO substrates as the working electrodes. The PTA solutions were replaced with 0.5 M NaCl aqueous solutions (pH 6.27) as the supporting electrolyte for water photolysis.[23] Localized acidification by the formation of hypochlorous acid (HClO) during photoelectrolysis establishes a pH of ∼2 in the vicinity of the WO_3 photoanode,[23] and thus it was not necessary to acidify the electrolyte. Therefore, an electrolyte pH approaching neutral can be used. The relevant reactions are

dx.doi.org/10.1021/jp400499c | J. Phys. Chem. C 2013, 117, 17766−17776

Table 1. Analytical Data Obtained from the Different Tests on the Films Deposited for 30 min from Pure PTA and PTA Containing 0.03 mol L^{-1} Carboxylic Acids

electrolyte composition	electrolyte pH	electrolyte conductivity (mS cm^{-1})	deposition time (min)	film thickness (nm)	microstructure	grain size (nm)[a]	true porosity (%)
PTA	1.71	2.900	30	653	large agglomerates	131	0.87
PTA + formic acid	1.70	3.120	30	700	small agglomerates	94	1.21
PTA + oxalic acid	1.41	6.570	30	1039	small agglomerates	83	1.91
PTA + citric acid	1.84	0.009	30	319	individual particles	45	3.78

[a]Measured using the line-intercept method (300 000× SEM images; 10 lines).

$$2NaCl \rightarrow 2Na^{+} + 2Cl^{-} \quad \text{in solution}$$

$$2Cl^{-} + 2h^{+} \rightarrow Cl_2 \quad \text{at the photoanode } (h^{+} \text{ is the photogenerated hole})$$

$$Cl_2 + H_2O \rightarrow HClO + HCl \quad \text{in solution}$$

The intensity of the incident light source (50 W tungsten-halogen lamp, chopped at a frequency of 0.05 Hz) used for exposure was measured with a light meter (Digitech QM1587) to be ~100 mW cm^{-2} (light source to film distance ~25 cm). Linear potentiodynamic photocurrent measurements were made at a scan rate of 5 mV s^{-1} and a step size of 1 mV.

3. RESULTS AND DISCUSSION

3.1. Effect of Types of Carboxylic Acid. Figure 1 shows the representative surface morphologies of the films deposited from pure PTA and PTA containing different carboxylic acids at constant concentrations. It is clear that there are three types of microstructures, viz., individual particles, small agglomerates, and large agglomerates, as summarized in Table 1. The individual particles consist of discrete grains with possible subgrains whereas the agglomerates are polycrystalline, containing multiple particles. The grain (agglomerate or particle) size effect is considered to result from a process similar to the deflocculation and dispersion of colloidal particles described by Sun et al. for WO_3 films prepared by oxalic acid-assisted colloid chemistry.[19,24] Carboxylic acids dissociate in aqueous solutions to form conjugate bases and hydronium ions.[25] These hydronium ions form hydrogen bonds with the highly electronegative oxygen atoms of PTA ions, thereby resulting in net positively charged states developed around the PTA ions, as shown in Figure 2. The interpretations of the effects of conjugate bases and hydronium ions bonded to the PTA ions (PTA–hydronium ion complexes) on the microstructures of the films are illustrated in Figure 3 and are as follows: (1) Pure PTA: large agglomerates of size ~131 nm (~500 nm max). In pure PTA, the absence of a separation effect by a deflocculation mechanism resulted in solute clustering and consequent rapid grain growth during annealing since the proximity of the ion complexes minimized the diffusion distances. (2) PTA containing 0.03 mol L^{-1} formic (oxalic) acid: small agglomerates of size ~94 nm (~83 nm). In PTA containing carboxylic acids whose conjugate bases have molecular weights of 45 g mol^{-1} (formate) and 125 g mol^{-1} (oxalate), (i) the hydronium ions caused deflocculation and (ii) the volumes occupied by the conjugate bases in solution contributed to some extent to increasing the degree of separation of the ion complexes. (3) PTA containing 0.03 mol L^{-1} citric acid: individual particles of size ~45 nm. In PTA containing citric acid, with a conjugate base of molecular weight 209 g mol^{-1}, deflocculation occurred, but the larger volume occupied by the citrate ions in solution effectively separated the ion complexes and increased the diffusion distance to the extent that little grain growth took place during annealing.

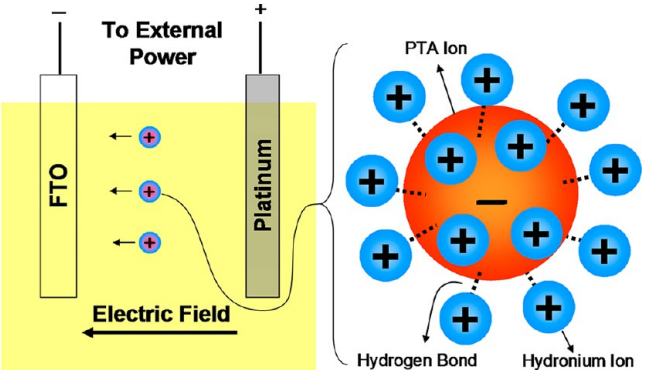

Figure 2. Schematic diagram of the effect of hydronium ions on positive charge imposition and consequent cathodic deposition.

In summary, it can be seen that the use of carboxylic acids is inevitably effective in facilitating deflocculation and suppressing solute clustering immediately before electrodeposition. The microstructures of the annealed films can be manipulated by using carboxylic acids of different molecular weights and associated sizes of conjugate bases, where the sizes of the conjugate bases control the distribution density of the WO_3 nuclei, their proximity, the corresponding diffusion distances, the tendency to undergo grain growth during annealing, and hence their susceptibility to forming solid agglomerates. Therefore, it is possible to obtain individual particles provided the conjugate bases are sufficiently large. It may be noted that the conjugate bases and hydronium ions were oxidized and effectively removed from the films upon annealing.

WO_3 exhibits an orthorhombic → monoclinic phase transformation upon cooling from ~330 °C, and this is associated with an extremely high thermal contraction of ~13 × 10^{-6} $°C^{-1}$ from this temperature to room temperature, measured both directly and calculated from the lattice parameters.[26,27] Although the high thermal contraction and the phase transformation experienced during cooling from 450 °C could be expected to facilitate delaminations between agglomerates, this is not supported by the observation that the film deposited from pure PTA (with the largest agglomerates) did not exhibit such delaminations. It is well known that agglomerates shrink independently during heating, so this also represents a possible mechanism of delamination.[28] Again, the

dx.doi.org/10.1021/jp400499c | J. Phys. Chem. C 2013, 117, 17766–17776

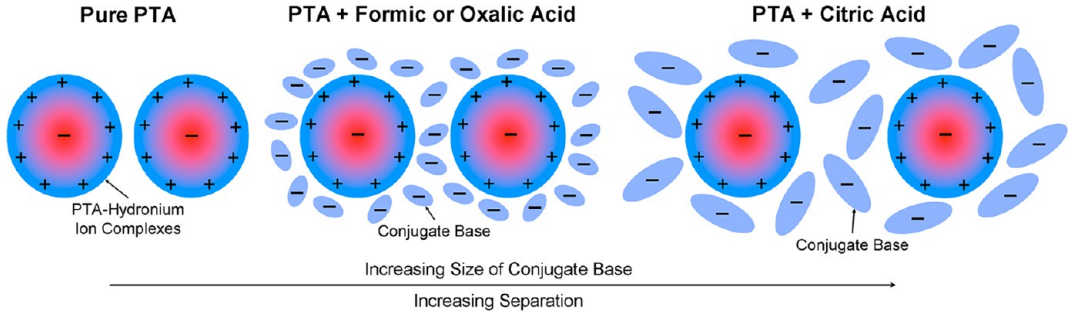

Figure 3. Illustration of the solute deflocculation effect from the hydronium ions and the separation effect from the conjugate bases for the different electrolyte compositions.

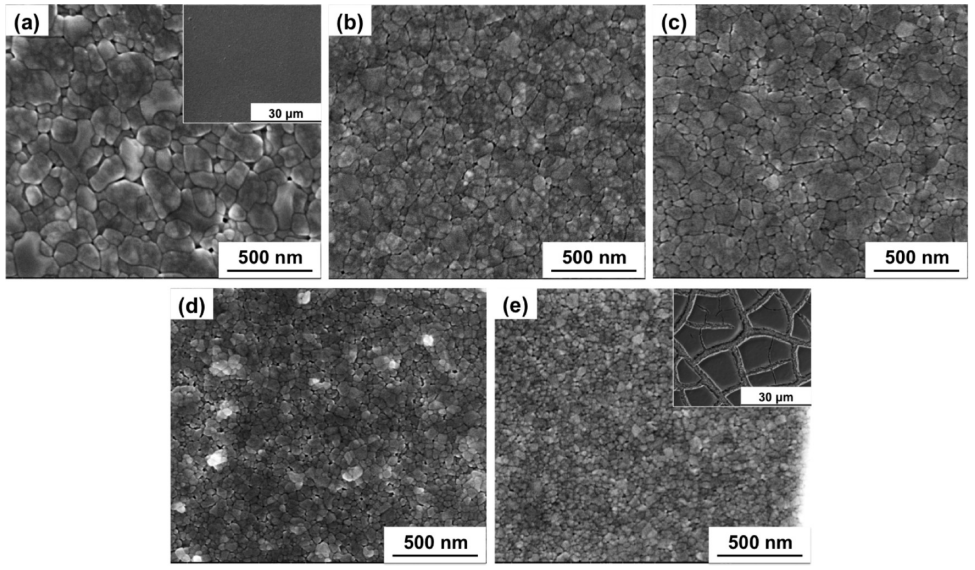

Figure 4. SEM images of WO_3 thin films deposited from (a) pure PTA and PTA containing oxalic acid at concentrations of (b) 0.01, (c) 0.03, (d) 0.05, and (e) 0.10 mol L^{-1}. Insets in a and e are at lower magnification.

SEM images in Figure 1 show that the largest agglomerates, which are in the film deposited from pure PTA, would be expected to show the largest annealing shrinkage, but no delaminations were observed.

These two observations support the conclusion of the importance of the separation effect by the conjugate bases. That is, for the film deposited from pure PTA, the absence of the conjugate bases allowed the close proximity of all particles, thereby facilitating effective intergranular bonding within and between agglomerates. For the films deposited from PTA containing formic or oxalic acid, the separation effect was such that effective bonding occurred within the agglomerates but thermal contraction and annealing shrinkage were sufficient to overcome the bonding between agglomerates. For the film deposited from PTA containing citric acid, the separation effect prevented agglomeration in the first place.

An examination of the true porosity data in Table 1 also supports the preceding conclusions. The film deposited from pure PTA had the lowest porosity, which consists of closed pores only. Despite the large agglomerate size, delaminations between agglomerates did not occur owing to the strong bonding between tightly packed agglomerates. In the films deposited with carboxylic acids, the porosities were increased by delaminations, which occurred owing to the separation effect of the conjugate bases. Hence, the porosity is a reflection of the separation effect: This separation effect on PTA containing formic acid (stronger bonding, fewer delaminations) was less than that on PTA containing oxalic acid (weaker bonding, more delaminations). With PTA containing citric acid, the largest conjugate base, the separation between individual particles was the greatest, so the porosity followed accordingly. In this case, delaminations were not apparent because the stress was evenly distributed throughout the particle network rather than along the agglomerate boundaries.

A comparison of the thicknesses of the films in Table 1, which were deposited for 30 min from pure PTA and PTA containing different carboxylic acids, shows that the deposition thicknesses increased, remained almost constant, and decreased (with respect to pure PTA) for the depositions done in PTA containing oxalic, formic, and citric acids, respectively. The same and reverse orders are seen in the respective case for the electrolyte conductivities and pH values. These observations suggest that the deposition thickness is a function of these two variables.

According to the pK_{a1} values (logarithm of the first proton acid dissociation constant) of the acids,[29−31] the degree of dissociation follows the order oxalic > citric > formic acid. The partial dissociation of formic acid produces a small number of hydronium ions and therefore minimally changed the electrolyte pH compared to that of pure PTA. The increase in the pH of PTA containing citric acid suggests that the pH was affected by hydrogen bonding between the highly electronegative

dx.doi.org/10.1021/jp400499c | J. Phys. Chem. C 2013, 117, 17766−17776

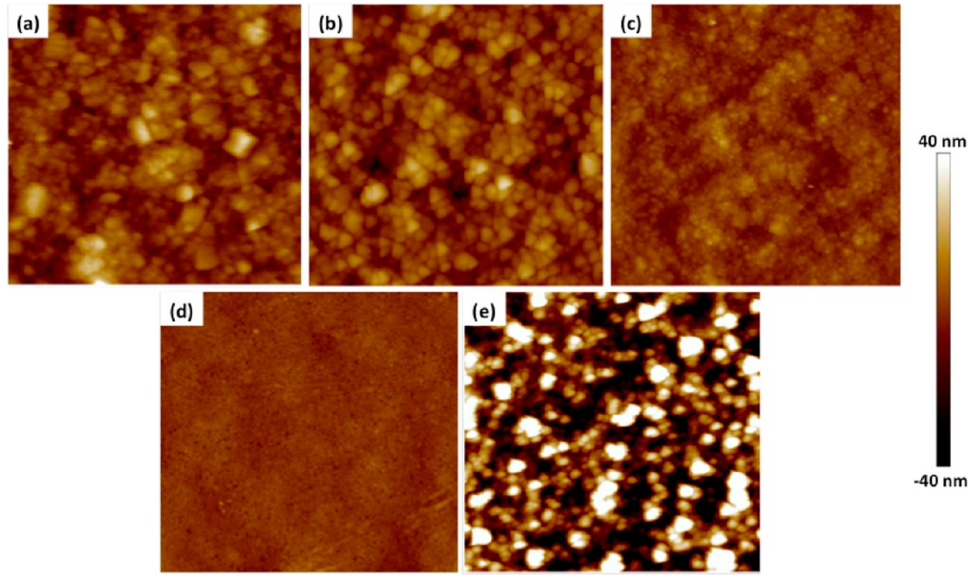

Figure 5. AFM images of WO_3 thin films deposited from (a) pure PTA and PTA containing oxalic acid at concentrations of (b) 0.01, (c) 0.03, (d) 0.05, and (e) 0.10 mol L^{-1}.

Table 2. Analytical Data Obtained from the Different Tests on the Films Deposited from Pure PTA and PTA Containing Oxalic Acid at Different Concentrations

film	oxalic acid concentration (mol L^{-1})	electrolyte pH	electrolyte conductivity (mS cm^{-1})	microstructure	grain size (nm)[a]	crystallite size(nm)[b]	true porosity (%)	(002) peak area	(020) peak area	(200) peak area	optical indirect band gap (eV)
A	0.00	1.71	2.90	large agglomerates	132	35	0.75	8052	1708	8885	2.90
B	0.01	1.49	5.06	small agglomerates	101	35	1.68	7997	1745	8071	2.90
C	0.03	1.41	6.57	small agglomerates	93	34	1.88	7177	1756	7780	2.95
D	0.05	1.35	8.35	small agglomerates	58	33	3.23	5281	1706	6566	3.05
E	0.10	1.25	12.50	individual particles	42	29	5.66	2700	1239	4066	3.30

[a]Measured using the line-intercept method (160,000× SEM images; 10 lines). [b]Measured using the Debye−Scherrer's equation by averaging (002), (020), and (200) crystallite sizes.

oxygen atoms of citrates and hydronium ions, thereby reducing the availability of hydronium ions. However, the dissociation of oxalic acid produces a large number of hydronium ions, as confirmed by the decreased electrolyte pH. This created highly net positively charged PTA ions resulting from the hydrogen bonding with the hydronium ions. Under cathodically biased conditions, the PTA ions were driven by the electric field to the working electrode, where they were reduced to form tungsten oxides, hence resulting in thicker films deposited in PTA containing oxalic acid.

Furthermore, it is clear that the molecular weights and associated sizes of the conjugate bases adversely affected the deposition thickness through molecular drag in the solutions. In this case, the order is citrate > oxalate > formate (molecular weights of the ions 209 > 125 > 45 g mol^{-1}). Since the effects of pK_{a1} values and molecular weights of the carboxylic acids show different trends with the electrolyte conductivity and pH, it is clear that they represent interdependent variables. The enhanced deposition thickness in PTA containing oxalic acid demonstrates that oxalic acid has the highest conductivity, the lowest pH, and the lowest pK_{a1} value, but its conjugate base does not have the lowest molecular weight. Therefore, it is concluded that the effect of the carboxylic acid is predominantly electrochemical and not physical, where the electrochemical factors are the pK_{a1} values of the acids and the resultant electrolyte conductivities and pH, whereas the physical factors are the molecular weights of the acids.

3.2. Effect of Concentrations of Oxalic Acid. Further studies on the effect of varying the oxalic acid concentrations were carried out by considering the advantages to a synthesis process yielding an enhanced deposition thickness from PTA containing oxalic acid. Higher concentrations of oxalic acid in PTA also resulted in increasing deposition thicknesses, which are attributed to the increasing availability of hydronium ions to form hydrogen bonds with the PTA ions. However, the initial trials revealed that longer deposition times resulted in cracked and poorly adhered thick films. To avoid this, films of similar thicknesses (400 ± 20 nm) were prepared where shorter deposition times (≤20 min) were applied to PTA containing higher oxalic acid concentrations. The films are named A−E according to their depositions from pure PTA and PTA containing 0.01, 0.03, 0.05, and 0.10 mol L^{-1} oxalic acid, respectively.

Figures 4 and 5 present the surface morphologies of the films deposited from pure PTA and PTA containing oxalic acid of different concentrations, as examined by SEM and AFM,

dx.doi.org/10.1021/jp400499c | J. Phys. Chem. C 2013, 117, 17766−17776

respectively. The scanned areas of the AFM images were 3 μm × 3 μm. The films consist of agglomerates/particles with sizes in the range of 42−132 nm, where the size decreases with increasing oxalic acid concentration (Table 2). Varying the oxalic acid concentration reveals that the separation effect of the conjugate bases is not only size-dependent but also depends on the amount present in the PTA electrolytes. Figure 4a,e shows insets at lower magnifications, illustrating the two characteristic types of larger-scale microstructures that were observed. The microstructure in Figure 4a is relatively homogeneous in terms of the grain size distribution and true porosity. Although this image is for the film A, it is similar to the images for films B−D. In contrast, Figure 4e shows a completely different microstructure of film E, consisting of isolated islands of unagglomerated particles that were generated by excessive shrinkage of the high-surface-area/energy particles (~39 nm) during annealing. The shrinkage appeared to have been so extreme that the microstructures of the islands are highly disrupted, with uneven steps and concavities. This is in contrast to the other agglomerated films, which consist of coarser particles of lower surface area/energy.[28]

Bruker NanoScope Analysis v1.4 software was used to analyze the AFM images of films A−E for information on the root-mean-square (rms) surface roughness and the surface area ratio (3D surface area/2D projected surface area).[21,32] The results have been plotted as a function of the grain size, as illustrated in Figure 6. Interestingly, the data for both the

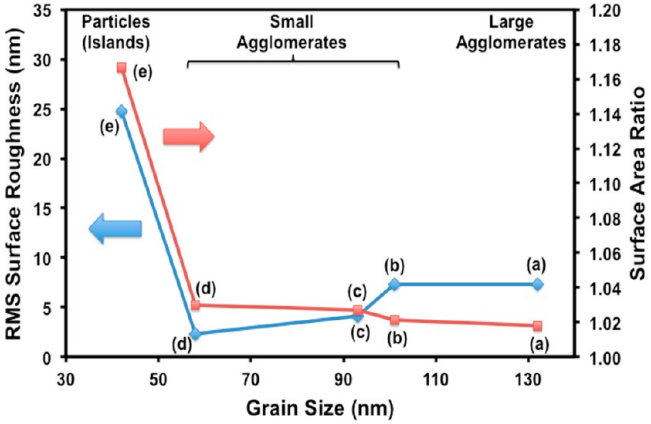

Figure 6. Root-mean-square surface roughnesses (blue ♦) and surface area ratios (red ■) as a function of the grain size of WO_3 thin films deposited from (a) pure PTA and PTA containing oxalic acid at concentrations of (b) 0.01, (c) 0.03, (d) 0.05, and (e) 0.10 mol L^{-1}.

surface area ratios and the rms surface roughness are bimodal. An abrupt increase in the specific surface area with decreasing grain size is observed at the transition from small agglomerates to particles, owing to the islandlike microstructure in Film E, as explained subsequently. A small grain is an advantage in terms of the specific surface area for photoelectrochemical applications, which depend on, inter alia, the number of reaction sites for water photolysis.[11]

At lower oxalic acid concentrations (≤0.05 mol L^{-1}), the rms surface roughness decreases from ~7 to ~2 nm with decreasing agglomerate size, as expected. In contrast, film E, which was deposited from PTA containing the highest oxalic acid concentration (0.10 mol L^{-1}) and consisting of small particles rather than fine agglomerates, gives an unexpectedly high roughness of ~24.80 nm. This results from the islandlike microstructure shown in Figure 4e, which caused the AFM tip to register the uneven steps and concavities created by the annealing shrinkage. For agglomerated films A−D, which were deposited from PTA containing ≤0.05 mol L^{-1} oxalic acid, the trend in the rms surface roughnesses is consistent with the work of other researchers with respect to WO_3 thin films synthesized by various methods and coarsened and agglomerated by annealing at 400−950 °C.[13,15,20,21,33]

Figure 7 shows the raw XRD results of the films deposited from pure PTA and PTA containing oxalic acid at different

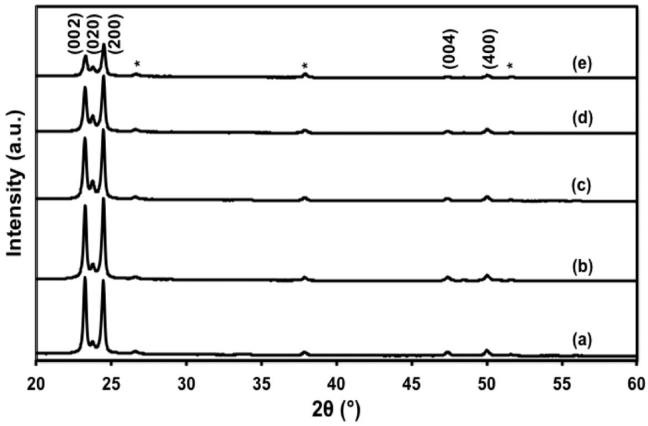

Figure 7. XRD spectra of monoclinic WO_3 thin films deposited from (a) pure PTA and PTA containing oxalic acid at concentrations of (b) 0.01, (c) 0.03, (d) 0.05, and (e) 0.10 mol L^{-1} (* FTO peaks).

concentrations, with major peaks at 23.3, 23.7, and 24.4° 2θ, which correspond to the (002), (020), and (200) planes of monoclinic WO_3,[34] respectively. The contributions of the FTO (positions, intensities, and full-widths at half-maxima) are approximately equivalent for all films, so a direct comparison of WO_3 films of variable thicknesses is facilitated. Compared to film A, films B−E show weaker and broader peaks with increasing oxalic acid concentrations. These data are consistent with the SEM images in Figure 4 and the data in Table 2. That is, true porosity controlled the peak intensities because it decreased the solid material area scanned by the X-ray beam. The grain size of <0.5 μm is much smaller than the beam diameter of 6.4−24 mm. The areas under the three main peaks scale in inverse proportion to the true porosities, as shown in Table 2.

In contrast, for colloidal WO_3 particles, Sun et al. observed that the particle size, degree of aggregation, and crystallinity decreased with increasing concentration of oxalic acid in the colloid suspension.[19] The first two observations were consistent with the role of the separation effect of the conjugate bases. The effect on crystallinity probably was not comparable because Sun et al. did not mention annealing their samples.[19]

The crystallite (subgrains comprising discrete grains) sizes of WO_3, as shown in Table 2, were estimated using the Debye−Scherrer equation by averaging those of the three major XRD reflections (002), (020), and (200).[35] The crystallite sizes are found to decrease from 35 to 29 nm with increasing oxalic acid concentration. The grain sizes, as suggested in Figure 4, show the same trend where they decrease from 132 to 42 nm for the same oxalic acid concentrations. These data show that the grains consist of multiple crystallites per grain (~3.8 crystallites/grain) in the absence of oxalic acid and approach

dx.doi.org/10.1021/jp400499c | J. Phys. Chem. C 2013, 117, 17766−17776

unity (~1.4 crystallites/grain) at the highest oxalic acid concentration.

Figure 8 shows the optical transmittance spectra of the films deposited from pure PTA and PTA containing oxalic acid at different concentrations. In general, films A–D, which were deposited from PTA containing ≤0.05 mol L^{-1} oxalic acid, absorb light in the near-UV region (<350 nm). Their optical absorption edges fall in the wavelength range of 350–450 nm. Relatively high transmittances (~60–80%) in the wavelength range of >450 nm are observed, and these are consistent for all of the films except for film E, which shows an indistinct optical absorption edge and very low transmittance owing to the scattering losses from its having the highest rms surface roughness and porosity resulting from the channels between the islands, uneven steps, and concavities.

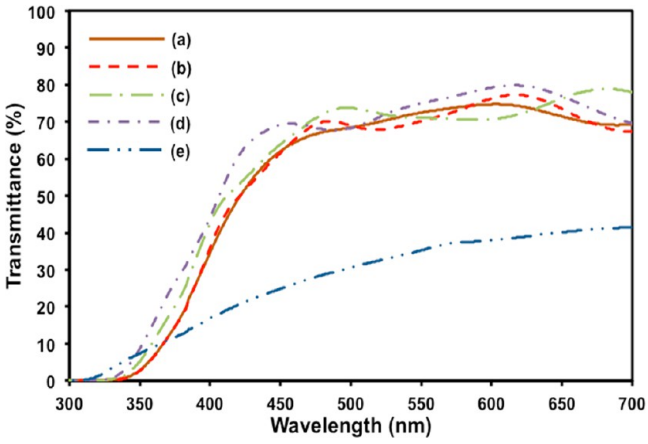

Figure 8. Transmittance spectra of WO_3 thin films deposited from (a) pure PTA and PTA containing oxalic acid at concentrations of (b) 0.01, (c) 0.03, (d) 0.05, and (e) 0.10 mol L^{-1}.

Blue shifts of <20 nm in the optical absorption edge, relative to film A, are observed in films B–D. The shifts follow the alphabetical order of the films, where film D shows the largest shift. This suggests that the optical band gaps of the films are dependent on the agglomerate/particle sizes. Tauc plots were used to obtain the optical indirect band gaps of the films, and the results are shown in Table 2.[36] The band gaps of the fabricated films vary in the range of 2.90–3.30 eV (wavelength range 376–428 nm). These values are significantly higher than the expected (theoretical) value of 2.60 eV for pure WO_3.[37] The principal reason for this is that the band gaps of thin films are dependent on their mineralogical and morphological characteristics, which in turn depend on the synthesis techniques employed. For electrodeposited WO_3 films with thickness in the range of ~250–1400 nm, the reported band gap values were 2.60–3.30 eV, with lower band gaps being measured for thicker films.[22,38,39] Similar trends between the band gap and film thickness also have been reported for WO_3 films synthesized using other techniques.[40−42] Films with band gaps close to the theoretical value have been reported to have typical thicknesses of several micrometers.[43−45] The main reason for these variations lies in the effect of residual stress on the thin films owing to thermal expansion mismatch between film and substrate as well as grain impingement in the film. Although these residual stresses give rise to structural imperfections and defects, which are known to affect the band gap,[22,46−50] these stresses decrease as the distance from the substrate to the film surface increases in thicker films, thus lowering the band gap. More generally, the relevant effects, including macrostructural and microstructural, on the band gap are as follows:

Bulk chemistry: All of the films had the same bulk composition, so this effect should not be relevant.

Defect chemistry: It is known that dopants affect the optical band gaps of materials.[51−53] Although no dopants were added, it was possible that contamination from Sn, F, Na, Ca, and/or Si might have occurred owing to diffusion from the FTO substrates during annealing. However, because all of the films were subjected to the same annealing conditions, this effect should be minimal or absent.

Mineralogy: There are five known atmospheric-pressure polymorphs of WO_3,[27] two of which are stable at room temperature (15–25 °C) and one of which could be quenched from the annealing temperature (450 °C). However, the X-ray diffraction data show that only the monoclinic polymorph is present, so this effect should not be relevant.

Macrostructure: The variations in structure, composition, and grain-impingement-induced compressive stress as a function of film thickness are known to affect the band gaps of materials.[22,46−50] However, because the film thicknesses are similar (400 ± 20 nm), this effect should not be significant.

Microstructure: The films consist of interconnected networks of grains in which the grain boundary areas (within the bulk and at the exposed surface) increase with decreasing grain size and increasing porosity. The increase in these grain boundary areas, which represent terminating structural and bonding regions and discontinuities in the lattice order, is known to increase the band gaps of materials.[12,18,24,54] Table 2 shows that the true porosity and the grain size vary with the amount of oxalic acid present in PTA. The associated variation in grain boundary areas would be expected to be relevant because these affect the proportion of defects.

In light of the preceding brief survey, it is probable that the principal factor affecting the band gap is the density of the defects associated with grain boundary areas.

3.3. Photoelectrochemical Tuning by Microstructural Control. The linear potentiodynamic photocurrent density measurements of the films deposited from pure PTA and PTA containing oxalic acid at different concentrations are shown in Figure 9. Effective photocurrents were measured as the

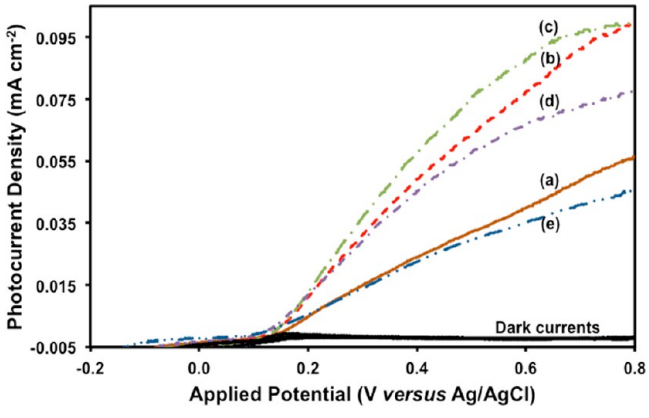

Figure 9. Linear potentiodynamic photocurrent densities of WO_3 thin films deposited from (a) pure PTA and PTA containing oxalic acid at concentrations of (b) 0.01, (c) 0.03, (d) 0.05, and (e) 0.10 mol L^{-1}; dark currents (measured without illumination) also are shown.

dx.doi.org/10.1021/jp400499c | J. Phys. Chem. C 2013, 117, 17766−17776

difference between photocurrents (with illumination) and dark currents (without illumination). It has been shown that the use of sodium chloride can stabilize the photoelectrochemical performance of WO_3 photoanodes by avoiding the formation of a passivating layer of peroxo (O−O) species on the surface of the photoanodes, which is favored when commonly used acids are employed as supporting electrolytes to lower the electrolyte pH.[23,55,56] It may be noted that up to ∼20% of the dark currents may be provided by chlorine gas formation ("...about 20% of the current efficiency.").[23] Also, because Xe light sources, which normally are used, and tungsten-halogen light sources produce significantly different spectral outputs, it is relevant to note that the integrated intensities of these two sources over the wavelengths absorbed below the minimal band gap of WO_3 film of ∼2.90 eV (∼428 nm) differ by a factor of approximately 50.[57] That is, the reported photocurrent densities were underestimated 50-fold (relative to the standard AM1.5G using a Xe light). Gaussian-shaped peaks, which correspond to electrochromic reactions of WO_3 films, are barely visible in the potentiodynamic scans in the present work owing to (i) the starting potential of −0.2 V versus Ag/AgCl, which is close to the peak potentials that occur in the typical range of ∼−0.2 V to −0.1 V versus Ag/AgCl,[32,58−60] and (ii) the relatively low scan rate of 5 mV s^{-1}, which is much lower than the typical rate of >50 mV s^{-1} reported in the literature.[61−64]

There were various microstructural (and structural) variables that influenced the photoelectrochemical results of the films, as summarized in Table 3. Decreasing grain sizes are beneficial in

Table 3. Effect of Decreasing Grain Size on Photoelectrochemical (PEC) Performance Factors and Associated Photocurrent Densities of WO_3 Thin Films

		effect of decreasing grain size on	
microstructural variable	PEC performance factor	PEC performance factor	photocurrent density
specific surface area	number of reaction sites	increase	increase
	number of recombination sites	increase	decrease
grain radius	hole transport	increase	increase
grain boundary distribution density	number of electron transport barriers	increase	decrease

(i) providing large specific surface areas and the associated number of reaction sites (oxygen vacancies)[65] for water photolysis and (ii) improving hole transport because the holes photogenerated in the outermost grains travel a shorter distance to the photoanode/electrolyte interface and oxidize water before they can recombine with the photogenerated electrons.[11] Vacancy filling by oxidation may degrade the photoelectrochemical activity owing to the reduced number of reaction sites.[66] The hole transport is moderated by the hopping distance, where long distances require more energy than short ones.[67] However, the large specific surface area also is associated with a high fraction of dangling bonds owing to the terminations of the crystal continuity.[68] These dangling bonds introduce deep localized levels in the energy band gap, which can trap photogenerated electron−hole pairs, thereby increasing their probabilities of surface recombination.[69,70] These undesirable dangling bonds may be removed by surface passivation.[69] For photogenerated electrons, the grain boundaries also act as weak links that hinder electron transport to the substrate.[71] It is well known that high-angle grain boundaries are associated with greater lattice mismatch and higher interfacial energies than low-angle grain boundaries.[28] Consequently, the greater the grain boundary angle, the weaker the link for electron transport.[72] The present work shows that these variables, which act concurrently, and their consequent influences on the photoelectrochemical performance of the films can be manipulated through grain size variation. The explanation of these data is as follows:

Pure PTA: Film A has the largest agglomerates (∼132 nm average; ∼500 nm maximum) and hence a relatively long hole diffusion distance and a limited specific surface area for both reaction and recombination sites. Across the film thickness of ∼400 nm, the number of agglomerates is ∼3, thus requiring the electrons to cross this relatively low number of transport barriers. This facilitates electron transport.

PTA containing 0.01−0.05 mol L^{-1} oxalic acid: Films B−D have small agglomerates (∼58−101 nm), so the hole diffusion distances are decreased. These small agglomerates also are associated with large specific surface areas for reaction sites. Nonetheless, these specific surface areas also are associated with a relatively high fraction of dangling bonds as recombination sites. The number of agglomerates in the cross section was ∼4−7, so the electrons must cross a greater number of transport barriers, which hinders electron transport.

PTA containing 0.10 mol L^{-1} oxalic acid: Film E has individual particles of ∼42 nm. The large specific surface area is associated with a high fraction of dangling bonds. This disadvantage is dominant over the advantages of a large number of reaction sites and a short hole diffusion distance. The intersection density of ∼10 agglomerates requires the electrons to cross a great number of transport barriers, thereby minimizing the electron transport.

The concept that condenses the main principles in terms of the size effect and the corresponding microstructural features that result in a maximum in the photocurrents is summarized schematically in Figure 10. Because the nuclei that precede crystallization are amorphous, they show negligible photocurrents,[54] and because single crystals have a minimal specific surface area, they show minimal photocurrents.[10] Therefore, it is clear that in microstructures that range from individual particles to small agglomerates to large agglomerates there must be a maximum in the photocurrent density. Hence, the observed maximum at a small agglomerate size of ∼90 nm corresponds to a balance between (i) the surface reaction and recombination sites and (ii) the hole and electron transports.

Similar bell-shaped relationships also have been observed by Li et al. and Hong et al.[12,13] Both observed optimal photoelectrochemical performance in WO_3 films consisting of what appeared to be small agglomerates of ∼60 nm size. The difference in the optimal size value could be the result of the different processing techniques employed in the synthesis of WO_3 films. These studies illustrated that the microstructures of these materials must be tuned so that the combination of the preceding four main photoelectrochemical performance factors can be optimized for maximal photoelectrochemical performance.

4. CONCLUSIONS

WO_3 thin films with controlled grain sizes (42−132 nm) were electrodeposited from PTA containing different carboxylic acids

dx.doi.org/10.1021/jp400499c | J. Phys. Chem. C 2013, 117, 17766−17776

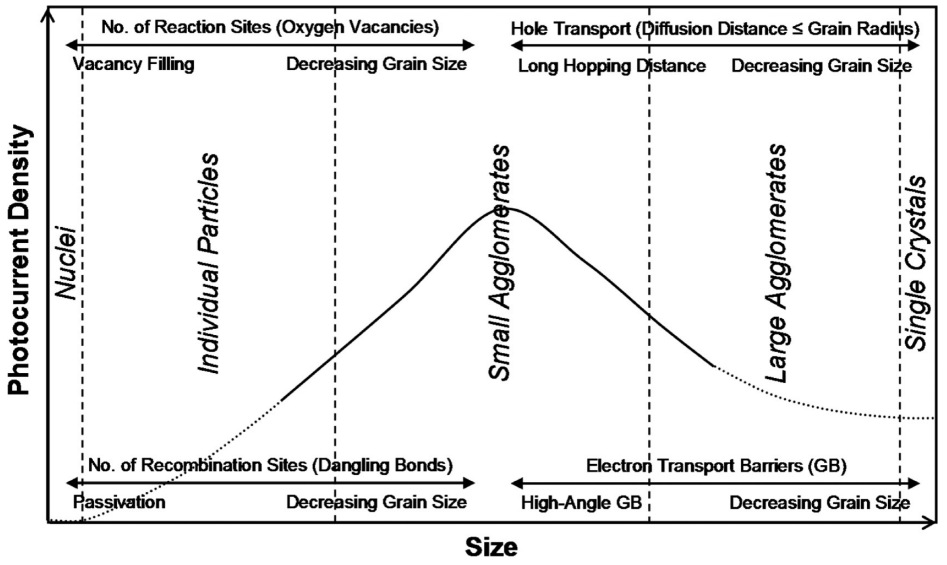

Figure 10. Schematic of the trend in the size effect on photocurrent density, where arrows indicate the effect of the fundamental microstructural feature (below arrows) on the photoelectrochemical performance factor (above arrows) (→ indicates an increase in the performance factor; ← indicates a decrease in the performance factor). The solid line (−) indicates experimental data, the dotted line (···) indicates extrapolation, and GB indicates grain boundaries.

(formic, oxalic, and citric). The electrodeposition of the films from PTA containing oxalic acid of different concentrations also was investigated. The deposition thickness was dependent on the electrolyte pH and electrical conductivity, both of which were dependent on the amount, degree of dissociation, molecular weight, and associated sizes of the acids. These influenced the availability of hydronium ions (for hydrogen bonding with PTA ions) and molecular drag in the electrolytes.

The morphological, mineralogical, optical, and photoelectrochemical properties of these films have been investigated. These data can be correlated through microstructural effects, viz., grain sizes and true porosities of the films. These effects were tunable through the use of carboxylic acids with different concentrations and sizes of conjugate bases, which contributed to the separation of the PTA ions, the distribution density of the WO_3 nuclei, their proximity, the corresponding diffusion distances, the tendency to undergo grain growth during annealing, and hence their susceptibility to forming agglomerates. The grain sizes decreased whereas the true porosities of the films increased with the increasing concentrations and sizes of the conjugate bases. These observations were consistent with the mineralogical data and were supported by the optical data in that the films consisting of smaller agglomerates/particles showed lower transmissions. These were consistent with the larger density of delaminations between particles and the greater amount of true porosity, which would scatter light maximally.

The nonlinear relationship between the grain sizes and the photoelectrochemical performance of WO_3 thin films suggested that the optimal photoelectrochemical performance of a film was a result of the tuning of (i) surface reaction and recombination sites and (ii) the hole and electron transports. The positive balance of the preceding photoelectrochemical performance factors resulted in a maximal photocurrent density at an agglomerate size of ∼90 nm, which was deposited from PTA containing 0.03 mol L^{-1} oxalic acid. Although it usually is assumed that nanomaterials with large specific surface areas are beneficial owing to the associated number of reaction sites, the present work shows that the optimization of the concurrent factors that affect the photoelectrochemical properties requires a more nuanced approach to processing. That is, small agglomerates appeared to offer a means of controlling the effective grain boundary area, which needs to be tuned between extremes.

AUTHOR INFORMATION

Corresponding Author

*E-mail: c.sorrell@unsw.edu.au. Tel: (+61-2) 9385-4421. Fax: (+61-2) 9385-6565.

Notes

The authors declare no competing financial interest.

ACKNOWLEDGMENTS

This work was supported in part by a project funded by the Australian Research Council (ARC). We are grateful for the characterization facilities from the Australian Microscopy & Microanalysis Research Facilities (AMMRF) node at the University of New South Wales (UNSW). W.L.K. gratefully acknowledges the receipt of a UNSW International Postgraduate Award to undertake this research degree.

REFERENCES

(1) Hodes, G.; Cahen, D.; Manassen, J. Tungsten Trioxide as a Photoanode for a Photoelectrochemical Cell (PEC). *Nature* **1976**, *260*, 312−313.

(2) Watcharenwong, A.; Chanmanee, W.; de Tacconi, N. R.; Chenthamarakshan, C. R.; Kajitvichyanukul, P.; Rajeshwar, K. Anodic Growth of Nanoporous WO_3 Films: Morphology, Photoelectrochemical Response and Photocatalytic Activity for Methylene Blue and Hexavalent Chrome Conversion. *J. Electroanal. Chem.* **2008**, *612*, 112−120.

(3) Shen, X. P.; Wang, G. X.; Wexler, D. Large-Scale Synthesis and Gas Sensing Application of Vertically Aligned and Double-Sided Tungsten Oxide Nanorod Arrays. *Sens. Actuators, B* **2009**, *143*, 325−332.

(4) Fang, F.; Kennedy, J.; Futter, J.; Hopf, T.; Markwitz, A.; Manikandan, E.; Henshaw, G. Size-Controlled Synthesis and Gas

Sensing Application of Tungsten Oxide Nanostructures Produced by Arc Discharge. *Nanotechnology* **2011**, *22*, 335702.
(5) Soliman, H. M. A.; Kashyout, A. B.; El Nouby, M. S.; Abosehly, A. M. Preparation and Characterizations of Tungsten Oxide Electrochromic Nanomaterials. *J. Mater. Sci.: Mater. Electron.* **2010**, *21*, 1313−1321.
(6) Li, W. J.; Fu, Z. W. Nanostructured WO_3 Thin Film as a New Anode Material for Lithium-Ion Batteries. *Appl. Surf. Sci.* **2010**, *256*, 2447−2452.
(7) Hanaor, D. A. H.; Triani, G.; Sorrell, C. C. Morphology and Photocatalytic Activity of Highly Oriented Mixed Phase Titanium Dioxide Thin Films. *Surf. Coat. Technol.* **2011**, *205*, 3658−3664.
(8) Liu, X.; Wang, F.; Wang, Q. Nanostructure-Based WO_3 Photoanodes for Photoelectrochemical Water Splitting. *Phys. Chem. Chem. Phys.* **2012**, *14*, 7894−7911.
(9) Li, Y.; Zhang, J. Z. Hydrogen Generation from Photoelectrochemical Water Splitting Based on Nanomaterials. *Laser Photonics Rev.* **2010**, *4*, 517−528.
(10) Santato, C.; Ulmann, M.; Augustynski, J. Enhanced Visible Light Conversion Efficiency Using Nanocrystalline WO_3 Films. *Adv. Mater.* **2001**, *13*, 511−514.
(11) Kelly, J. J.; Vanmaekelbergh, D. Porous-Etched Semiconductors: Formation and Characterization. In *Electrochemistry of Nanomaterials*; Hodes, G., Ed.; Wiley-VCH: Weinheim, Germany, 2001; pp 103−139.
(12) Li, W.; Li, J.; Wang, X.; Ma, J.; Chen, Q. Photoelectrochemical and Physical Properties of WO_3 Films Obtained by the Polymeric Precursor Method. *Int. J. Hydrogen Energy* **2010**, *35*, 13137−13145.
(13) Hong, S. J.; Jun, H.; Borse, P. H.; Lee, J. S. Size Effects of WO_3 Nanocrystals for Photooxidation of Water in Particulate Suspension and Photoelectrochemical Film Systems. *Int. J. Hydrogen Energy* **2009**, *34*, 3234−3242.
(14) Sun, X. L.; Cao, H. T.; Liu, Z. M.; Li, J. Z. Influence of Annealing Temperature on Microstructure and Optical Properties of Sol-Gel Derived Tungsten Oxide Films. *Appl. Surf. Sci.* **2009**, *255*, 8629−8633.
(15) Su, P. G.; Pan, T. T. Fabrication of a Room-Temperature NO_2 Gas Sensor Based on WO_3 Films and WO_3/MWCNT Nanocomposite Films by Combining Polyol Process with Metal Organic Decomposition Method. *Mater. Chem. Phys.* **2011**, *125*, 351−357.
(16) White, C. M.; Jang, J. S.; Lee, S. H.; Pankow, J.; Dillon, A. C. Photocatalytic Activity and Photoelectrochemical Property of Nano-WO_3 Powders Made by Hot-Wire Chemical Vapor Deposition. *Electrochem. Solid-State Lett.* **2010**, *13*, B120−B122.
(17) Vemuri, R. S.; Bharathi, K. K.; Gullapalli, S. K.; Ramana, C. V. Effect of Structure and Size on the Electrical Properties of Nanocrystalline WO_3 Films. *ACS Appl. Mater. Interfaces* **2010**, *2*, 2623−2628.
(18) Gullapalli, S. K.; Vemuri, R. S.; Ramana, C. V. Structural Transformation Induced Changes in the Optical Properties of Nanocrystalline Tungsten Oxide Thin Films. *Appl. Phys. Lett.* **2010**, *96*, 171903.
(19) Sun, M.; Xu, N.; Cao, Y. W.; Yao, J. N.; Wang, E. G. Preparation, Microstructure and Photochromism of a New Nanocrystalline WO_3 Film. *J. Mater. Sci. Lett.* **2000**, *19*, 1407−1409.
(20) Meda, L.; Tozzola, G.; Tacca, A.; Marra, G.; Caramori, S.; Cristino, V.; Bignozzi, C. A. Photo-Electrochemical Properties of Nanostructured WO_3 Prepared with Different Organic Dispersing Agents. *Sol. Energy Mater. Sol. Cells* **2010**, *94*, 788−796.
(21) Naseri, N.; Yousefzadeh, S.; Daryaei, E.; Moshfegh, A. Z. Photoresponse and H_2 Production of Topographically Controlled PEG Assisted Sol-Gel WO_3 Nanocrystalline Thin Films. *Int. J. Hydrogen Energy* **2011**, *36*, 13461−13472.
(22) Kwong, W. L.; Savvides, N.; Sorrell, C. C. Electrodeposited Nanostructured WO_3 Thin Films for Photoelectrochemical Applications. *Electrochim. Acta* **2012**, *75*, 371−380.
(23) Augustynski, J.; Solarska, R.; Hagemann, H.; Santato, C. Nanostructured Thin-Film Tungsten Trioxide Photoanodes for Solar Water and Sea-Water Splitting . *Proc. SPIE* **2006**, *6340*, 63400J.
(24) Sun, M.; Xu, N.; Cao, Y. W.; Yao, J. N.; Wang, E. G. Nanocrystalline Tungsten Oxide Thin Film: Preparation, Microstructure, and Photochromic Behavior. *J. Mater. Res.* **2000**, *15*, 927−933.
(25) Kotz, J. C.; Treichel, P. M.; Townsend, J. R. *Chemistry and Chemical Reactivity*; Brooks/Cole: Belmont, CA, 2010.
(26) Sawada, S.; Ando, R.; Nomura, S. Thermal Expansion and Specific Heat of Tungsten Oxide at High Temperatures. *Phys. Rev.* **1951**, *84*, 1054−1055.
(27) Lassner, E.; Schubert, W. D. *Tungsten: Properties, Chemistry, Technology of the Element, Alloys, and Chemical Compounds*; Kluwer Academic/Plenum Publishers: New York, 1999.
(28) Kingery, W. D.; Bowen, H. K.; Uhlmann, D. R. *Introduction to Ceramics*; John Wiley and Sons: New York, 1976.
(29) Barile, F. A. *Principles of Toxicology Testing*; CRC Press: Boca Raton, FL, 2008.
(30) Bettelheim, F. A.; Brown, W. H.; Campbell, M. K.; Farrell, S. O. *Introduction to Organic and Biochemistry*; Brooks/Cole: Belmont, CA, 2010.
(31) Armstrong, J. *General, Organic, and Biochemistry: An Applied Approach*; Brooks/Cole: Belmont, CA, 2012.
(32) Vernardou, D.; Drosos, H.; Spanakis, E.; Koudoumas, E.; Savvakisab, C.; Katsarakis, N. Electrochemical and Photocatalytic Properties of WO_3 Coatings Grown at Low Temperatures. *J. Mater. Chem.* **2011**, *21*, 513−517.
(33) Xin, G.; Guo, W.; Ma, T. Effect of Annealing Temperature on the Photocatalytic Activity of WO_3 for O_2 Evolution. *Appl. Surf. Sci.* **2009**, *256*, 165−169.
(34) Woodward, P. M.; Sleight, A. W.; Vogt, T. Structure Refinement of Triclinic Tungsten Trioxide. *J. Phys. Chem. Solids* **1995**, *56*, 1305−1315.
(35) Waseda, Y.; Matsubara, E.; Shinoda, K. *X-ray Diffraction Crystallography: Introduction, Examples and Solved Problems*; Springer: New York, 2011.
(36) Tauc, J. Optical Properties and Electronic Structure of Amorphous Ge and Si. *Mater. Res. Bull.* **1968**, *3*, 37−46.
(37) Koffyberg, F. P.; Dwight, K.; Wold, A. Interband Transitions of Semiconducting Oxides Determined from Photoelectrolysis Spectra. *Solid State Commun.* **1979**, *30*, 433−437.
(38) Hechavarria, L.; Hu, H.; Miranda, M.; Nicho, M. E. Electrochromic Responses of Low-Temperature-Annealed Tungsten Oxide Thin Films in Contact with a Liquid and a Polymeric Gel Electrolyte. *J. Solid State Electrochem.* **2009**, *13*, 687−695.
(39) Monllor-Satoca, D.; Borja, L.; Rodes, A.; Gómez, R.; Salvador, P. Photoelectrochemical Behavior of Nanostructured WO_3 Thin-Film Electrodes: The Oxidation of Formic Acid. *ChemPhysChem* **2006**, *7*, 2540−2551.
(40) Azimirad, R.; Akhavan, O.; Moshfegh, A. Z. Influence of Coloring Voltage and Thickness on Electrochromical Properties of E-Beam Evaporated WO_3 Thin Films. *J. Electrochem. Soc.* **2006**, *153*, E11−E16.
(41) Johansson, M. B.; Baldissera, G.; Valyukh, I.; Persson, C.; Arwin, H.; Niklasson, G. A.; Osterlund, L. Electronic and Optical Properties of Nanocrystalline WO_3 Thin Films Studied by Optical Spectroscopy and Density Functional Calculations. *J. Phys.: Condens. Matter* **2013**, *25*, 205502.
(42) Kalagi, S. S.; Mali, S. S.; Dalavi, D. S.; Inamdar, A. I.; Im, H.; Patil, P. S. Transmission Attenuation and Chromic Contrast Characterization of R.F. Sputtered WO_3 Thin Films for Electrochromic Device Applications. *Electrochim. Acta* **2012**, *85*, 501−508.
(43) Su, J.; Feng, X.; Sloppy, J. D.; Guo, L.; Grimes, C. A. Vertically Aligned WO_3 Nanowire Arrays Grown Directly on Transparent Conducting Oxide Coated Glass: Synthesis and Photoelectrochemical Properties. *Nano Lett.* **2011**, *11*, 203−208.
(44) Qin, D. D.; Tao, C. L.; Friesen, S. A.; Wang, T. H.; Varghese, O. K.; Bao, N. Z.; Yang, Z. Y.; Mallouk, T. E.; Grimes, C. A. Dense Layers of Vertically Oriented WO_3 Crystals as Anodes for Photoelectrochemical Water Oxidation. *Chem. Commun.* **2012**, *48*, 729−731.

(45) Ng, C.; Ye, C. H.; Ng, Y. H.; Amal, R. Flower-Shaped Tungsten Oxide with Inorganic Fullerene-Like Structure: Synthesis and Characterization. *Cryst. Growth Des.* **2010**, *10*, 3794−3801.
(46) Mohanty, B. C.; Jo, Y. H.; Yeon, D. H.; Choi, I. J.; Cho, Y. S. Stress-Induced Anomalous Shift of Optical Band Gap in ZnO:Al Thin Films. *Appl. Phys. Lett.* **2009**, *95*, 062103.
(47) Marotti, R. E.; Guerra, D. N.; Bello, C.; Machado, G.; Dalchiele, E. A. Bandgap Energy Tuning of Electrochemically Grown ZnO Thin Films by Thickness and Electrodeposition Potential. *Sol. Energy Mater. Sol. Cells* **2004**, *82*, 85−103.
(48) Pandiaraman, M.; Soundararajan, N.; Vijayan, C. Effect of Thickness on the Optical Band Gap of Silver Telluride Thin Films. *J. Ovonic Res.* **2011**, *7*, 21−27.
(49) Goh, E. S. M.; Chen, T. P.; Sun, C. Q.; Liu, Y. C. Thickness Effect on the Band Gap and Optical Properties of Germanium Thin Flms. *J. Appl. Phys.* **2010**, *107*, 024305.
(50) Weinhardt, L.; Blum, M.; Bar, M.; Heske, C.; Cole, B.; Marsen, B.; Miller, E. L. Electronic Surface Level Positions of WO_3 Thin Films for Photoelectrochemical Hydrogen Production. *J. Phys. Chem. C* **2008**, *112*, 3078−3082.
(51) Cole, B.; Marsen, B.; Miller, E.; Yan, Y. F.; To, B.; Jones, K.; Al-Jassim, M. Evaluation of Nitrogen Doping of Tungsten Oxide for Photoelectrochemical Water Splitting. *J. Phys. Chem. C* **2008**, *112*, 5213−5220.
(52) Tang, J.; Wang, D.; Zou, Z.; Ye, J. Modification of Photophysical Properties of WO_3 by Doping Different Metals. *Mater. Sci. Forum* **2003**, *423*−*425*, 163−166.
(53) Sun, Y.; Murphy, C. J.; Reyes-Gil, K. R.; Reyes-Garcia, E. A.; Thornton, J. M.; Morris, N. A.; Raftery, D. Photoelectrochemical and Structural Characterization of Carbon-Doped WO_3 Films Prepared via Spray Pyrolysis. *Int. J. Hydrogen Energy* **2009**, *34*, 8476−8484.
(54) Diquarto, F.; Dipaola, A.; Piazza, S.; Sunseri, C. Influence of Thermal-Treatment on the Photoelectrochemical Behavior of WO_3 Photoanodes Electrochemically Grown. *Sol. Energy Mater.* **1985**, *11*, 419−433.
(55) Alexander, B. D.; Augustynski, J. Nanostructured Thin-Film WO_3 Photoanodes for Solar Water and Sea-Water Splitting. In *On Solar Hydrogen and Nanotechnology*; Vayssieres, L., Ed.; John Wiley and Sons: Singapore, 2009; pp 342−345.
(56) Ulmann, M.; Detacconi, N. R.; Augustynski, J. Behavior of Surface Peroxo Species in the Photoreactons at TiO_2. *J. Phys. Chem.* **1986**, *90*, 6523−6530.
(57) Yoo, W. S.; Kang, K. Electrical Activation of Ultra-Shallow B and BF_2 Implanted Silicon by Flash Anneal. *Nucl. Instrum. Methods Phys. Res., Sect. B* **2005**, *237*, 12−17.
(58) Deepa, M.; Kar, M.; Singh, D. P.; Srivastava, A. K.; Ahmad, S. Influence of Polyethylene Glycol Template on Microstructure and Electrochromic Properties of Tungsten Oxide. *Sol. Energy Mater. Sol. Cells* **2008**, *92*, 170−178.
(59) Ahn, K. S.; Lee, S. H.; Dillon, A. C.; Tracy, C. E.; Pitts, R. The Effect of Thermal Annealing on Photoelectrochemical Responses of WO_3 Thin Films. *J. Appl. Phys.* **2007**, *101*, 093524.
(60) Liao, C. C.; Chen, F. R.; Kai, J. J. Electrochromic Properties of Nanocomposite WO_3 Films. *Sol. Energy Mater. Sol. Cells* **2007**, *91*, 1282−1288.
(61) García-Cañadas, J.; Mora-Seró, I.; Fabregat-Santiago, F.; Bisquert, J.; Garcia-Belmonte, G. Analysis of Cyclic Voltammograms of Electrochromic a-WO_3 Films from Voltage-Dependent Equilibrium Capacitance Measurements. *J. Electroanal. Chem.* **2004**, *565*, 329−334.
(62) Shiyanovskaya, I.; Hepel, M.; Tewksburry, E. Electrochromism in Electrodeposited Nanocrystalline WO_3 Films I. Electrochemical and Optical Properties. *J. New Mater. Electrochem. Syst.* **2000**, *3*, 241−247.
(63) Kim, D. H. Effects of Phase and Morphology on the Electrochromic Performance of Tungsten Oxide Nano-Urchins. *Sol. Energy Mater. Sol. Cells* **2012**, *107*, 81−86.
(64) Zhang, J.; Wang, X. L.; Xia, X. H.; Gu, C. D.; Tu, J. P. Electrochromic Behavior of WO_3 Nanotree Films Prepared by Hydrothermal Oxidation. *Sol. Energy Mater. Sol. Cells* **2011**, *95*, 2107−2112.
(65) Wendt, S.; Vang, R. T.; Besenbacher, F. Fundamental Reactions on Rutile TiO_2 (110) Model Photocatalysts Studied by High-Resolution Scanning Tunneling Microscopy. In *On Solar Hydrogen and Nanotechnology*; Vayssieres, L., Ed.; John Wiley and Sons: Singapore, 2009.
(66) Wang, S.; Verma, A.; Yang, Y. L.; Jacobson, A. J.; Abeles, B. The Effect of the Magnitude of the Oxygen Partial Pressure Change in Electrical Conductivity Relaxation Measurements: Oxygen Transport Kinetics in $La_{0.5}Sr_{0.5}CoO_{3-d}$. *Solid State Ionics* **2001**, *140*, 125−133.
(67) Feng, D.; Jin, G. *Introduction to Condensed Matter Physics*; World Scientific Publishing: Singapore, 2005.
(68) Pai, M. R.; Banerjee, A. M.; Tripathi, A. K.; Bharadwaj, S. R. *Functional Materials: Preparation, Processing and Applications*; Elsevier: Waltham, MA, 2012.
(69) Yacobi, B. G. *Semiconductor Materials: An Introduction to Basic Principles*; Kluwer Academic/Plenum Publishers: New York, 2003.
(70) Mendis, B. G.; Bowen, L.; Jiang, Q. Z. A Contactless Method for Measuring the Recombination Velocity of an Individual Grain Boundary in Thin-Film Photovoltaics. *Appl. Phys. Lett.* **2010**, *97*, 092112.
(71) Deutscher, G. Origin of Weak-Link Behavior of Grain Boundaries in Superconducting Cuprates and Pnictides. *Appl. Phys. Lett.* **2010**, *96*, 122502.
(72) Yau, J. K. F.; Sorrell, C. C. High-J_c $(Bi,Pb)_2Sr_2Ca_2Cu_3O_{10+x}$ Tapes Fabricated by Electrophoretic Deposition. *Physica C* **1997**, *282*−*287*, 2563−2564.